




Generating functionally graded steel microstructures by laser powder bed fusion

Aron Pfaff^{1,*} , Markus Linnenberg¹, Klaus Hoschke¹, and Frank Balle^{1,2,3}

¹ Fraunhofer Institute for High-Speed Dynamics, Ernst-Mach-Institut, Ernst-Zermelo-Str. 4, 79104 Freiburg, Germany

² Department for Sustainable Systems Engineering (INATECH),

Walter and Ingeborg Herrmann Chair for Engineering of Functional Materials (EFM), University of Freiburg, Freiburg, Germany

³ Freiburg Materials Research Center (FMF), Stefan-Meier-Str. 21, 79104 Freiburg, Germany

Received: 19 June 2023

Accepted: 24 October 2023

Published online:
20 November 2023

© The Author(s), 2023

ABSTRACT

Laser Powder Bed Fusion (L-PBF) is bearing the potential to generate new functionally graded microstructures (FGMi) whose properties are tailored regarding specific applications. However, locally altering the process parameters in order to create such microstructures can easily compromise the relative mass density and therefore the performance of a material. This work presents and investigates in situ heat treatments by double exposure in order to realize FGMi. The results show an increased parameter flexibility without compromising the relative mass density, when compared to a single exposure of the investigated low-alloy steel 30CrMoNb5-2. The systematic investigation regarding the impact of process parameters enables microstructures in the hardness range from approx. 380–510 HV10. Especially, the introduction of cooling breaks between single exposure tracks increases the hardness of the microstructure. Tensile tests show an increase in UTS by 21.3%, when comparing the results with a nonin situ heat treated sample (single exposure). A homogeneously in situ heat treated sample as well as both discrete and continuously graded samples demonstrate the potential of the novel method. Consequently, the presented double exposure approach for in situ heat treatments is offering a new flexibility regarding the creation of FGMi by L-PBF and will therefore support the development of future high-performance materials.

Handling Editor: Sophie Primig.

Address correspondence to E-mail: aron.pfaff@emi.fraunhofer.de

E-mail Addresses: frank.balle@inatech.uni-freiburg.de

<https://doi.org/10.1007/s10853-023-09086-y>

Introduction

Motivation and potential field of application

Functionally Graded Materials (FGM) present a group of materials whose properties are tailored regarding specific applications. Tailored FGM bears the potential to increase the local performance of a component as well as to reduce its weight. In addition, the durability could be increased, resulting in an increased material efficiency and resilience. FGM are based on a varying composition or structure [1–4]. As shown by Pandey [3], FGM can be classified in the following three groups: porosity gradients (e.g., foams), compositional or chemical gradient (e.g., hard/carbide metals) and graded microstructures. The latter, referred to as Functionally Graded Microstructures (FGMi), is based on the fact that the microstructure such as grain size, orientation or phase distribution of a material is determining its behavior [1, 2]. A good and common example is the blade of a knife. While the cutting edge requires a high hardness in order to create a sharp blade, other areas however should show increased ductility. Since these properties pose a classical trade-off scenario in material engineering, areas of different microstructures are created resulting in an FGMi.

The combination of geometrical design freedom and the potential to create metal-based FGMi makes additive manufacturing (AM) an interesting candidate in order to create new materials for kinetic energy absorption. Many examples (e.g., [5–8]) show the potential of complex geometries like lattice structures or foams for energy absorption under different load cases like crash, impact or blast. Other works show the potential of FGMi or FGM created by conventional local heat treatments for energy absorption (e.g., see [9–12]). Simoes et al. [13] demonstrate the importance of L-PBF process parameter choice for lattice structures under dynamic loads. Pfaff et al. [14] further design the local adaption of process parameters to generate FGMi in combination with the new geometrical design freedom of AM. Given the background of energy absorption under dynamic loads, steels present an interesting group of alloys, since they can offer constant high tensile strength in combination with high strains. Low-alloy steels also offer several possibilities regarding the creation of FGMi. While different phases and grain sizes can theoretically be generated by different cooling rates, the martensitic state also offers the potential to create areas of different tempering states.

Therefore, the low-alloy steel “30CrMoNb5-2” with a chemical composition of 0.29C-0.91Cr-0.73Mn-0.33Ni-0.27Mo-0.26Si-0.05Cu-0.04Al (wt. %) is investigated within this work.

State of the art of functionally graded microstructures by metal additive manufacturing

The microstructure of a material depends on its thermomechanical history and therefore on the manufacturing process and its process parameters used to create and form it. There are different conventional manufacturing processes which can be used to create FGMi under certain process limitations, as shown by Kieback et al. and Rasheedat et al. [15, 16]. However, due to its incremental nature, AM poses less limitations and enables more flexibility compared to other processes and therefore has the biggest potential to create metallic FGMi [2, 16, 17]. The microstructure of each incremental element within AM depends on the specific local boundary conditions [18]. In the case of Laser Powder Bed Fusion (L-PBF), which presents one of the best-established metal-AM technology to date [19], the microstructure and thus the mechanical properties mainly depend on the solidification process of the melt pool as well as thermal loads resulting from the exposure of following process layers. L-PBF consists of approximately 50 [20] to 130 [21] process parameters. Several of these impact the material's microstructure and consequently its mechanical properties [22].

The literature shows different approaches in order to create FGMi by metal-AM. Kürsteiner et al. [23] for example are introducing an approach where the directed energy deposition (DED) process is being stopped between layers in order to cool down the component. These interruptions increase the cooling rates in the following layer. Martensitic instead of austenitic areas are the result, when processing a maraging steel. Also, L-PBF can be used to create local changes in phase composition using a 17–4 PH steel as shown by Freeman et al. [24, 25]. By changing the cooling duration through variations in hatch distance, exposure speed and exposure diameter, paramagnetic austenitic and ferromagnetic martensitic regions have been realized. Zrodowski et al. [26] even present the possibility to create classical crystalline phases next to amorphous regions based on different cooling rates within L-PBF. Popowich et al. [27, 28] in contrast

are using Ni-based Inconel alloys and varying laser power, exposure speed, hatch distance and layer thickness within the L-PBF process in order to create local changes in grain size and therefore in hardness or yield strength. Also, Nematollahi et al. [29] show that a change in laser power and scanning speed will result in different material properties when manufacturing NiTi shape memory alloys. Donik et al. [30] investigate the impact of the energy density onto the grain size, hardness and tensile properties for 316 L. The results prove that weak changes in material properties are possible if the relative mass density has to be kept stable. Niendorf et al. [31] prove for a Fe–Mn–Al–Ni steel that also the area of the exposure cross section is impacting the thermal boundary conditions, resulting in a change of cooling rates and therefore grain size and orientation. The results of Hearn et al. [32] indicate that tempering effects can be controlled by process parameter variations, when processing low-alloy steels. Double-, multi-, re-melting- or so-called repetitive exposure strategies can improve densification, surface roughness or reduce material defects (e.g., see [33–38]). Onal et al. [39] observe that a double exposure on Ti–6Al–4 V can result in a more uniform, finer and thus harder microstructure. Also, AlMangour et al. [40] show that a double exposure can result in finer dendrites when processing TiC/316 L stainless steel nanocomposites. Zhan et al. [41] use double exposure to tune the phase transformation behavior and mechanical properties for NiTi shape memory alloys.

Context of this work

As demonstrated by the studies above, different process parameters and approaches can be used to impact the microstructure regarding grain size, grain orientation or phase distribution. However, improving the material performance by microstructural changes, also means to achieve an at least nonsignificant negative change in porosity. Most publications do not address this problem, but seem to result in increased porosity when looking into the presented images. As shown by Donik et al. [30], Zhang et al. [42], and Kumar et al. [43], some alloys like 316 L and Inconel 718 offer a relatively wide parameter range without causing excessive porosities. However, even though Inconel 718 presents a rather good tolerance toward parameter changes, the results of Popowich et al. [27] show an increase in porosity by 245% due

to process parameter variations. The significance of such an porosity increase is given by Kan et al. [44]. Other alloys can show a more limited process window as shown by Calignano et al. [45], Pfaff et al. [46] and Yadroitsev et al. [47]. Hence, the necessary process parameter changes in order to achieve significant microstructural changes compromise the relative mass density and therefore material performance. Example for this limitation is given by Donik et al. [30] for 316 L and Pfaff et al. [48] for AlSi10Mg. It is also known for low-alloy steels that slight parameter changes can lead to defects like cracks and porosities [49]. Preliminary studies regarding the investigated low-alloy steel show similar limitation (see Sect. “Flexibility of primary exposure parameters”).

Within this work, a double exposure approach is being presented in order to increase the variability of process parameters and resulting microstructure without compromising the relative mass density in order to achieve an increased material performance. This approach can be used to realize in situ heat treatments in order to create FGMi. Furthermore, it can be utilized to create first FGMi based on a continuous property gradient. In contrast, all current studies presented above are based on sudden, discontinuous changes in material properties.

Materials and methods

Machine, equipment and preparation

The powder was manufactured by gas atomization (argon) and characteristics are analyzed by high-speed imaging using a “Camsizer X2”. The measured particle size distribution is illustrated by the $D_{10/50/90}$ values indicating that 10/50/90% of the particles have an even or smaller diameter than the presented value. The results present D_{10} , D_{50} and D_{90} values of 6.63 μm , 29.18 μm , and 49.75 μm , respectively. The typical particle morphology is illustrated within Fig. 1. The powder is processed using a “EOS M100” L-PBF system and under a layer thickness of 30 μm . Argon 4.6 shielding gas resulting in a maximum oxygen content of 0.1% is applied. The used 200 W cw-laser enables a maximum laser power of 170 W within the built chamber has a wavelength of 1070 nm and a non-variable focus diameter of 40 μm based on a Gaussian profile regarding the energy density. The powder bed is not heated, and rotating marcelled laser tracks are used

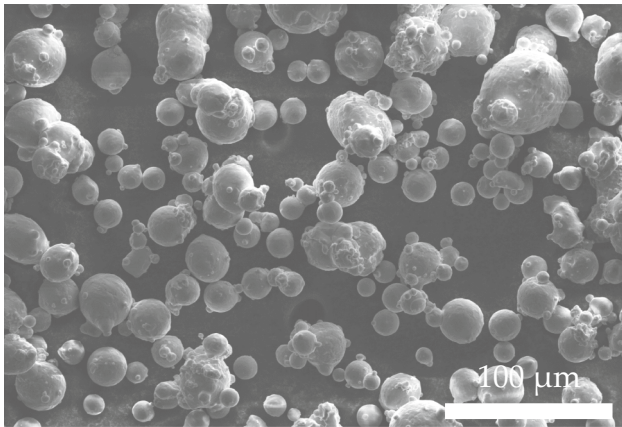


Figure 1 SEM image of the used steel powder.

as an exposure strategy. Hardness measurements are carried out by a microhardness tester from “Leitz Wetzlar” using the Vickers method (HV 0.1; load: 0.9807 N, time: 14 s). Macro-hardness (HV 1; load: 98.07 N, time: 14 s) is measured using a “Q250” from Qness following DIN EN ISO 6507-1. Plain grinding of the cross section specimens is followed by fine grinding with grit sizes and diamond sprays of 15 μm , 9 μm , 3 μm up to 1 μm . All samples were prepared for light optical microscopy (LOM) using Nital etching. Mass densities were measured based on the Archimedes principle using 1 cm^3 cubic samples and a Kern ABT 220-5DM. Tensile tests at room temperature were executed on round tensile specimens (\varnothing 4 mm; length reduced section: 30 mm) according to DIN EN ISO 6892 using an Instron 8033. The engineering strain was measured by single camera digital image correlation using “GOM Correlate”. EBSD measurements were conducted using a DigiView 5 camera integrated into a Zeiss Evo 15. The step width of the measurements was set to 0.5 μm .

Methodology for in situ heat treatment

In a first step within this work, the process parameter development and the limitations regarding process parameter variability are being presented, followed by investigations regarding the approach shown in Fig. 2.

The double exposure approach presents a possibility to increase process parameter flexibility without compromising the relative mass density of a material. A *primary exposure* is being applied to each process layer in order to achieve a maximum relative mass density (see Fig. 2a). Each laser track is exposed

in direct succession to the previous one. The time between each laser track Δt_p is typically set to a minimum, resulting in an increased temperature of the component during the exposure as shown by João et al. [50].

A *secondary exposure* parameter is applied in order to re-melt certain areas of the material (Fig. 2b). The purpose of this exposure is to control the cooling rate within the melt track by the parameter variations as well as the heat treatment of surrounding and underlying material. Δt_s presents the time between each secondary laser track. Inspired by works like Cheloni et al. [50] or Kürsteiner et al. [23], it is assumed that an increased Δt_s will result in a lower thermal load in underlying areas as well as increased cooling rates regarding the melt pool of the secondary exposure. Since the primary exposure of following process layers will re-melt underlying areas, the melt pool depth of the secondary exposure should be preferably deeper than the one of the primary. Based on experience and the DED results of Kürsteiner et al. [23] it is assumed that Δt_s presents a major parameter regarding the FGMi design by L-PBF. The secondary exposure parameters can be chosen with an increased flexibility, since they are applied to an already dense bulk material. This assumption is based on the following knowledge:

Lack-of-fusion (LOF), balling, and keyhole formation are the three main defect modes resulting in porosities. For instance, the power density of a laser used in keyhole mode causes evaporations, which result in a cavity, which again boosts laser absorption. The result is a deeper melt pool than possible by a purely conduction-driven mode. Characteristic spherical voids within the laser track are the outcome, as demonstrated by Madison [51]. Balling refers to a periodic oscillation of the width of the melt pool tracks caused by instable melt pools, whereas LOF is caused by insufficient penetration into the substrate, resulting in large and sharp pores [22, 52]. Regarding the secondary exposure parameters, LOF is not relevant anymore, since the bulk material is already consisting of fused layers. Keyholing phenomena are expected to be harder to trigger, since even without evaporations the initial state of a powder layer is already consisting of gas cavities. This should cause an increased absorption of already reflected radiation (interparticle reflections see [53]) leading to deep welding. Therefore, the parameter threshold to trigger keyholing should be lower, when exposing bulk material. Furthermore, it

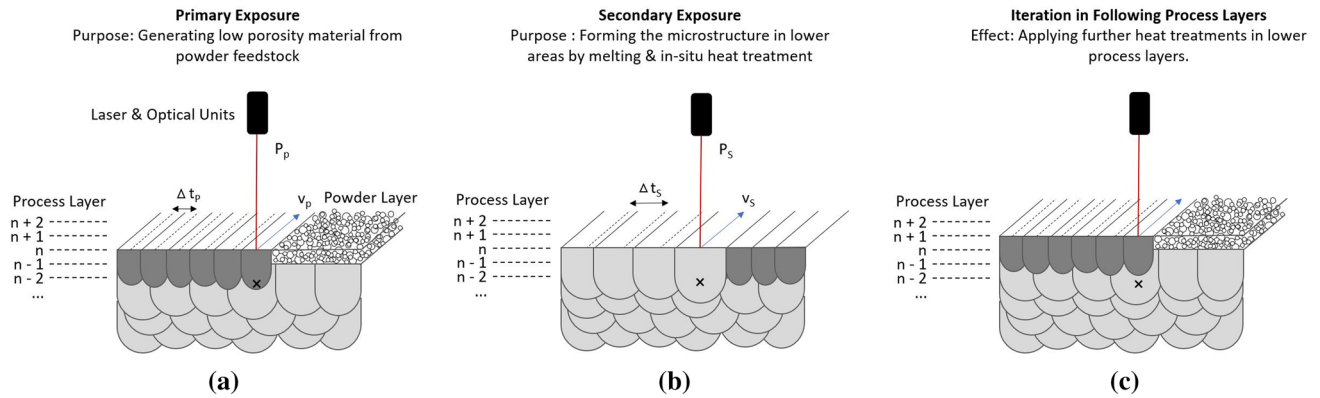


Figure 2 Proposed approach in order to create functionally graded steel microstructures of maximum relative mass density by in situ heat treatments via double exposure. **a** Primary expo-

sure of powder layer, **b** secondary exposure of bulk material, **c** iteration of **a** and **b** in following process layers.

can be expected that bulk material is showing a lower tendency to balling phenomena than a layer of powder, since the available material is distributed more smoothly, which supports the stability of melt tracks.

While the primary exposure is applied in each process layer, the secondary exposure is not necessarily applied in each layer. However, not only the secondary exposure will form the resulting microstructure but also the exposure of following process layers. Both exposures will lead to a heat treatment of material in underlying layers. Hearn et al. [32] for example observe a micro- and macro-tempering of martensite in lower process layers in the case of low-alloy steels. Microstructural analyses in order to verify changes in mechanical behavior are time consuming, intricate in interpretation and prone to errors, due to the expectable phases, which are all based on body-centered crystal structures (e.g., martensite, bainite, ferrite). Therefore, micro-hardness measurements are used within this work, in order to identify relevant changes in microstructure. This is done based on the correlation of microstructures, hardness and the stress/strain properties [54, 55]. While a hardness value only presents a semi-quantitative measure of resistance to plastic deformation, it still shows correlations to the tensile properties and microstructure within a material class. This has been shown for many alloys (e.g., [56–59]) and can also be observed for low-alloy steels as shown by the ASTM A 370–68 steel table. However, a direct statement between the properties is not possible [54]. The assumptions and presented approach above result in the following hypotheses for this work:

Hypothesis 1 Variations in primary exposure parameters can lead to (microstructural) changes in hardness but also compromise the relative mass density.

Hypothesis 2 The double exposure approach increases the variability of process parameters for in situ heat treatments, without compromising the relative mass density.

Hypothesis 3 Introducing cooling phases (Δt) between single exposure tracks will facilitate microstructures of increased hardness.

Results and discussions

Development and characterization of primary exposure parameters

Process parameter development

The primary exposure parameters were developed based on the approaches presented by Pfaff et al. [46] and Johnson et al. [52] for a layer thickness of $l = 30 \mu\text{m}$. Figure 3a, b presents the measured melt pool dimensions. The width of the melt pool (W), the depth (D), the length (L), and the layer thickness (l) are the four categories that are used in literature to describe the scope of Keyholing, LOF and Balling [46, 52, 60–62]. The printability map (Fig. 3c) is retrieved based on the following threshold values defined by Johnson et al. [52]: Keyholing $W/D < 1.5$, LOF $D/l < 1.5$ und Balling $L/W > 2.3$.

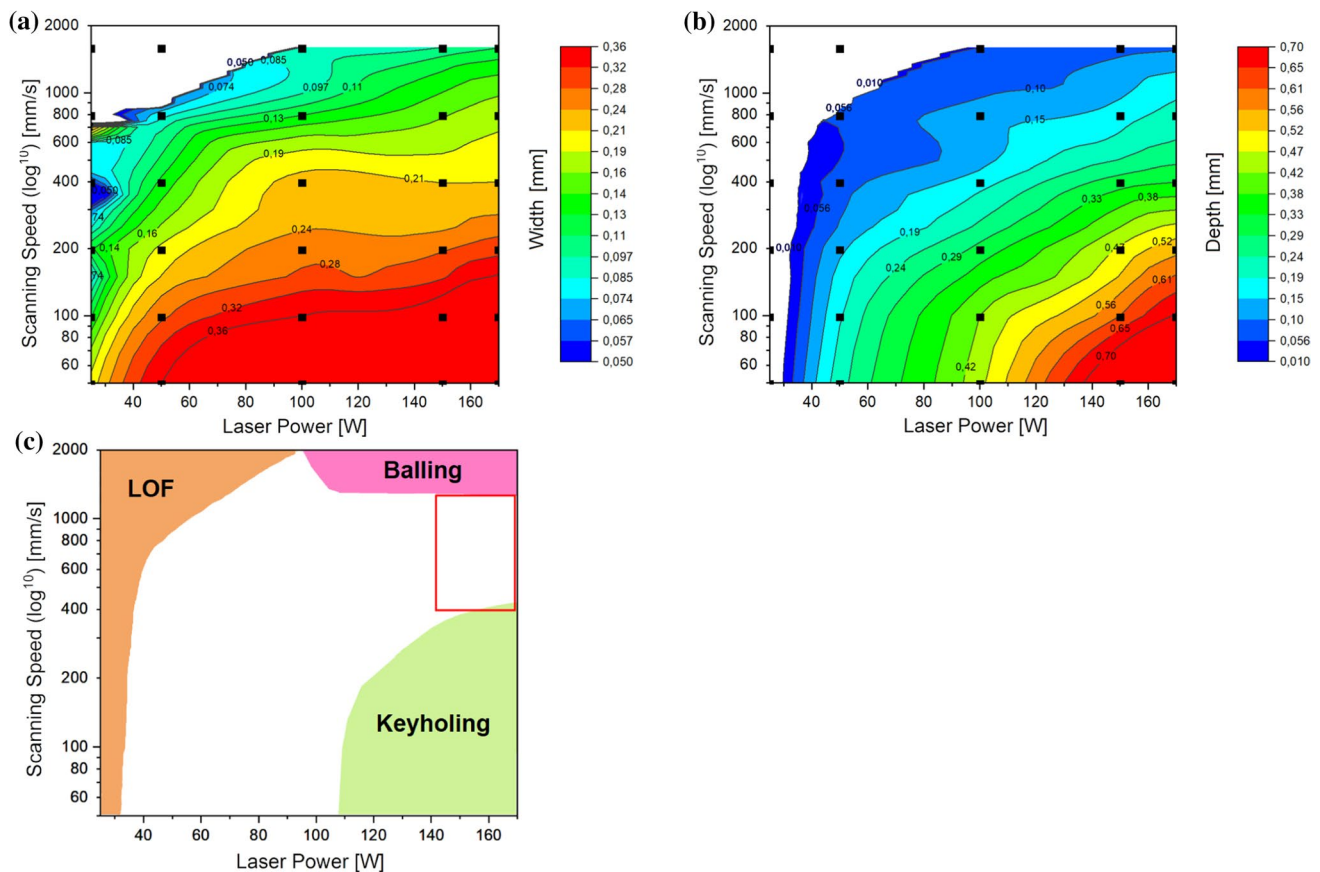


Figure 3 Melt pool dimensions of single laser tracks. **a** Melt pool width. **b** Melt pool depth. **c** Printability map based on the following threshold values: Keyholing $W/D < 1.5$, Lack-of-Fusion

(LOF) $D/t < 1.5$ und Balling $L/W > 2.3$. Marked in red: Investigated area for volumetric L-PBF process parameters

Based on the printability map in Fig. 3b, a Design of Experiment (DoE) plan was conducted within the following process window, as marked in Fig. 3b in red: Laser power P_p 140–170 W; exposure speed v_p 400–1400 mm/s; hatch distance h_p 0.06–0.1 mm. Based on a 5% level of significance, the resulting model equation shows a good coefficient of determination ($R^2 = 88.89$). The relative mass density is retrieved based on an absolute density of 7.86 g/cm^3 based on Lide [63]. In a second iteration, the window was limited to the range of highest density (140–170 W and 800–1100 mm/s), while setting the least significant factor “hatch distance” to 0.08 mm. This second iteration results in a coefficient of determination $R^2 = 86.73$. Both resulting model equations are visualized in Figs. 4 and 5. In the course of the third iteration, only the exposure speed is varied by the values 860, 880, 900 and 920 mm/s. The laser power remains at 170 W, the path distance at 0.08 mm. For each variation, 4 samples were produced. No significant variation was detected

using t tests. The maximum relative mass density was measured at 880 mm/s. Based on these findings, primary exposure parameters are set to 170 W, 880 mm/s and 0.08 mm. A density of 7.82 g/cm^3 ($\sigma = 0.0043$) or 99.5% was determined. Visual evaluation by LOM of cross section specimens reveal similar relative densities of 99.6% ($\sigma = 0.091$). Hardness tests yield a value of 395.96 HV ($\sigma = 7.17$) or 410 HBW ($\sigma = 5$).

Flexibility of primary exposure parameters

The laser power, exposure speed, hatch distance as well as Δt (time between laser tracks) are assumed to enable the highest potential to impact the cooling rates and in situ heat treatments and are therefore investigated. Regarding the first three a DoE based on a CCC-Design plan was placed around the primary exposure parameter. The parameters within the design plan were varied by $\pm 2.5\%$ in a

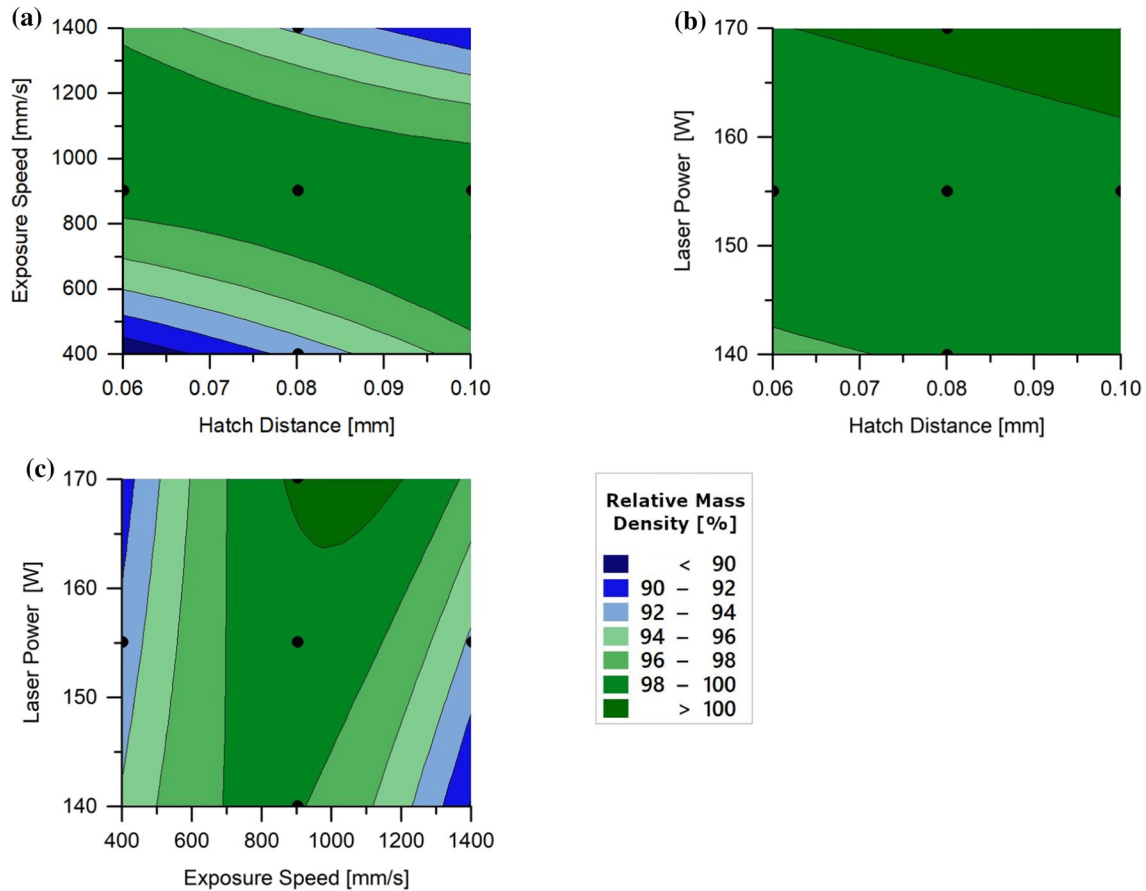


Figure 4 Visualization of the first DoE iteration. Points of measurement are marked by black dots. Model equation: $\rho(P,v,h) = 89.2 - 0.258P + 0.0192v + 368h - 0.000024v^2 - 0.391hv + 0.000365vP$.

a Exposure speed vs. hatch distance (hold value 155 W). **b** Laser power vs. hatch distance (hold value 900 mm/s). **c** Laser power vs. exposure speed (hold value 0.08 mm).

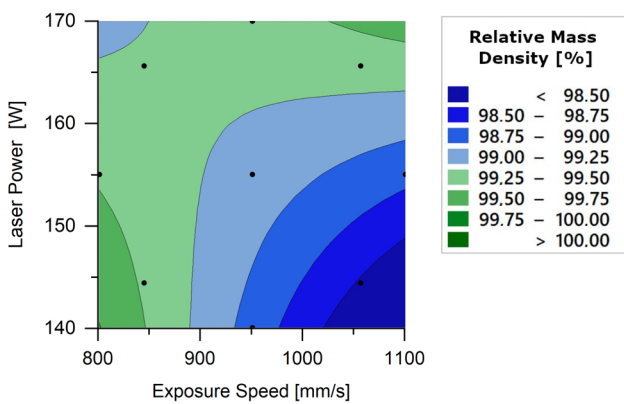


Figure 5 Visualization of the second DoE iteration. Points of measurement are marked by black dots. Model equation: $\rho(P,v,h) = 261.8 - 0.97P - 0.1872v + 0.001117vP$.

first step, followed by variation of $\pm 5\%$ and $\pm 7.5\%$. At a variation of $\pm 7.5\%$, the exposure speed showed a first significant impact above the defined level of significance of 5%. The measurements in Fig. 6a visualize the effect by a direct change of exposure speed and therefore energy density. These results also show that the porosities cannot be prevented by an adaptation of the hatch distance. Regarding the resulting hardness, no significant impact is observed for changes in energy density (via exposure speed) and hatch distance (see Fig. 6b). All samples so far are based on a direct temporal succession of laser tracks. Hence, a minimum Δt_p is necessary for the sky writing process (turn around and acceleration path) and is being applied. Regarding the measurements in Fig. 6b, d, Δt_p is set to ~ 1 s. The results show a surprisingly strong impact on the porosity. Due to the high porosity, the relative mass density

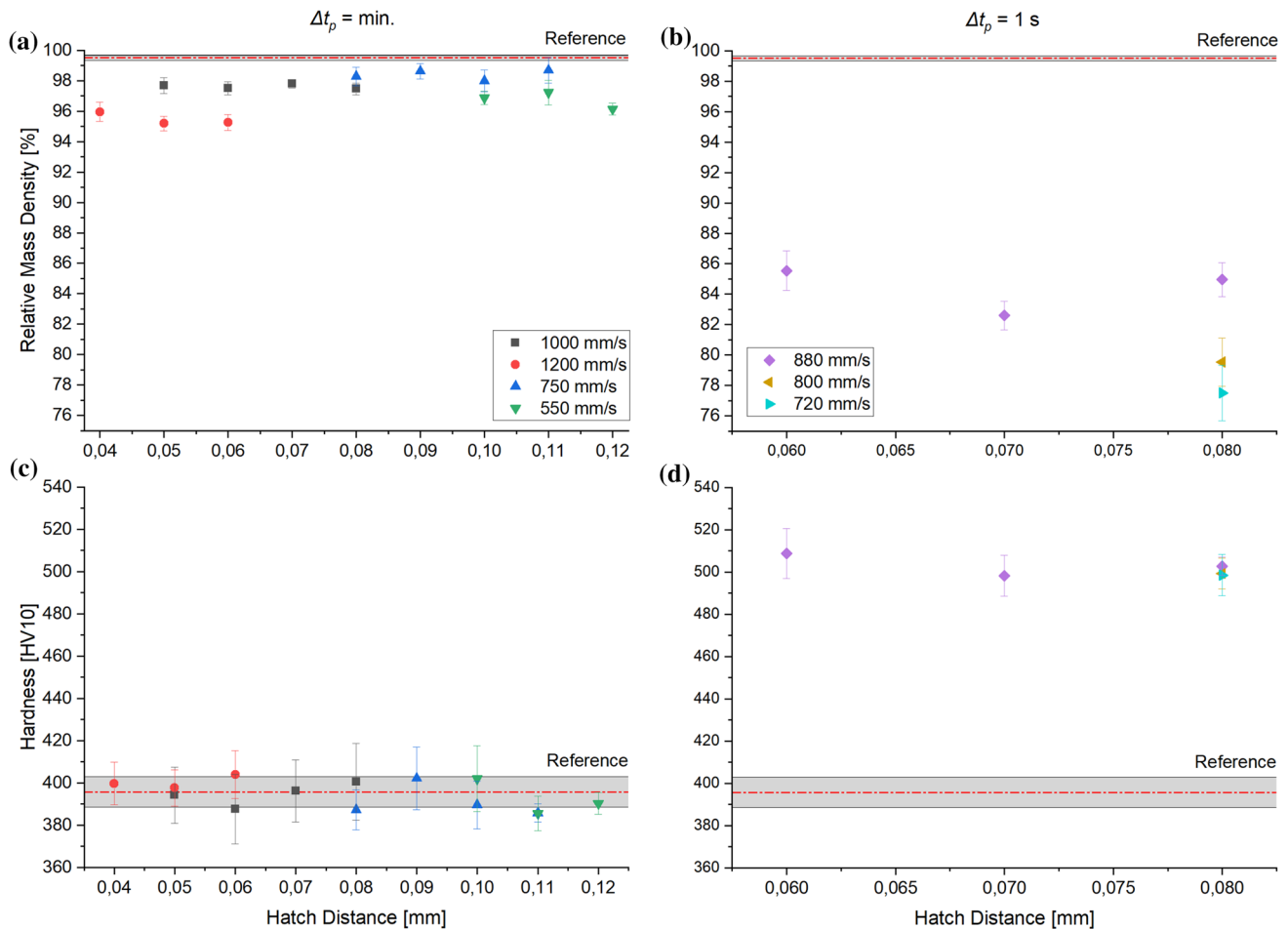


Figure 6 Flexibility of primary exposure parameters regarding the resulting porosity and hardness. Each standard deviation is based on a group size of four samples. **a** Impact of changes in exposure speed (energy density) and adapted hatch distance on

relative mass density at $P_p = 170 \text{ W}$; $\Delta t \approx \text{min.}$ **c** Corresponding hardness values. **b** Relative mass density of samples manufactured at $\Delta t_p \approx 1 \text{ s}$; $P_p = 170 \text{ W}$. **d** Corresponding hardness values.

was measured by LOM imaging instead of by the Archimedes principle. At $P_p = 170 \text{ W}$, $v_p = 880 \text{ mm/s}$, $h_p = 0.08 \text{ mm}$ and $\Delta t_p = 1 \text{ s}$, only Δt_p is changed compared to the reference parameters resulting in a decrease in approx. 15 pp. Adaptions in exposure speed or hatch distance do not eliminate this trend. Changes in Δt_p result in an increase from approx. 396 HV10 to approx. 500 HV10. Attempts to increase the relative mass density reproducibly back to approx. 99.5% by applying the secondary exposure were unsuccessful.

Proof of Hypothesis 1 The results above show that the flexibility regarding energy density and hatch distance is not sufficient for changes in hardness without significantly compromising the relative mass density.

Variations regarding Δt_p also proof that microstructural changes are possible by variations in primary exposure parameters, increasing the hardness from 396 to approx. 500 HV10 but also result in a distinct loss in relative mass density ($\sim 15 \text{ pp}$).

Expectations regarding Hardness based on Single Laser Track Experiments

Figure 7 presents the microhardness measured within single laser tracks. Two states labeled as “HT” and “no HT” are measured (definition see Fig. 7a). “No HT” presents laser tracks placed within the final exposure layers. Therefore, no heat treatment resulting from consecutive layers was applied. “HT” presents laser tracks, which were placed within the

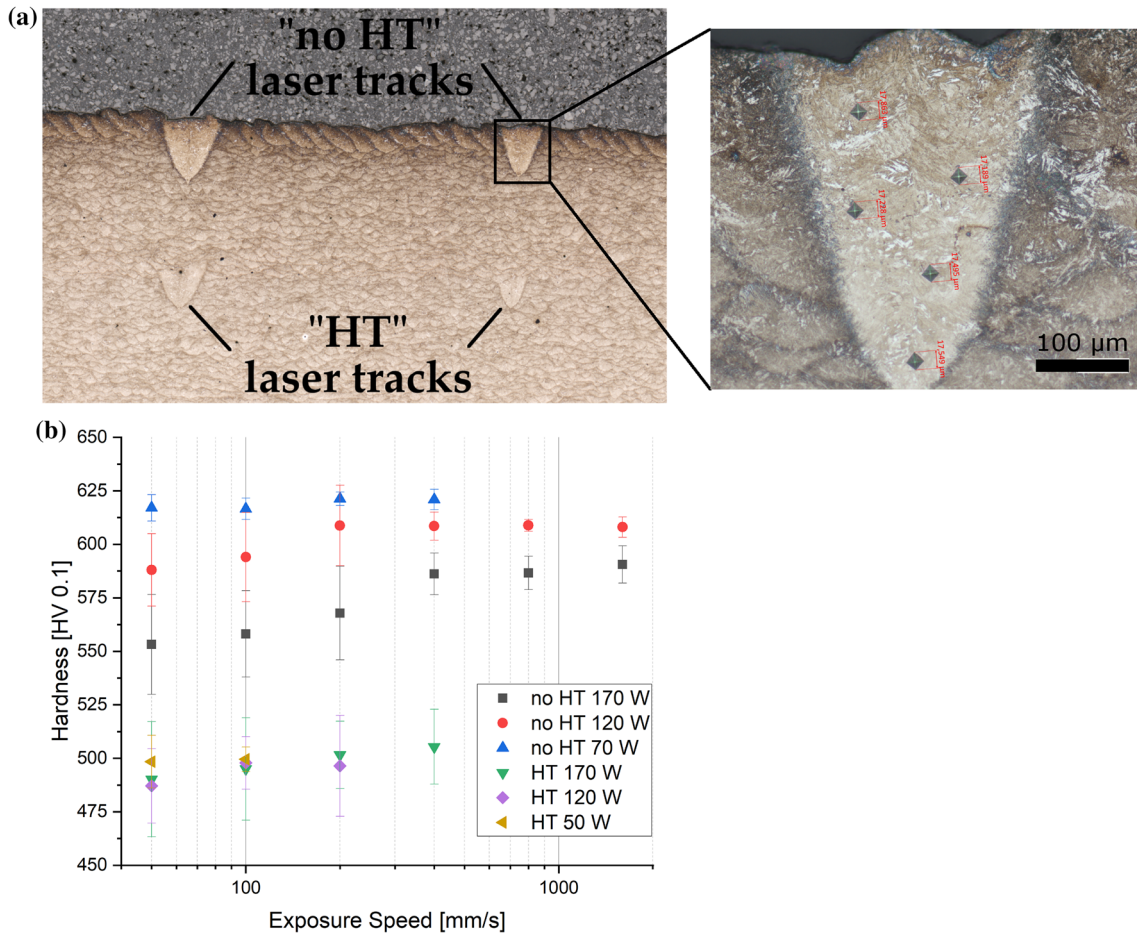


Figure 7 Micro-hardness measured on single laser tracks. **a** Image of the investigated cross section sample showing the position of the single laser tracks to demonstrate the definition of “no HT” (no in situ heat treatment; single laser track placed in final exposure layer) and “HT” (in situ heat treatment; single

laser track placed in material, followed by exposure layers). Right hand side: Exemplary measurement within single laser track (170 W; 400 mm/s; “no HT”). **b** Microhardness measured on the two states “no HT” and “HT”.

material. For this group, an in situ heat treatment has been applied through consecutive process layers exposed by the primary exposure. Each laser track was measured up to five times throughout its cross section as shown in Fig. 7a.

“No HT” laser tracks within the last process layer reach a maximum of approx. 620 HV0.1. Laser tracks of a higher laser power show lower hardness increasing with the exposure speed. The values converge around 400 mm/s. The standard deviation increases with the melt pool cross section (increasing laser power; decreasing exposure speed). A tendency of a softer core and harder values toward the edges was observed, which is in accordance with the thermal gradient during melting and solidification (e.g., see

[64]). As described by Xia et al. [64], increased melt pool dimensions show stronger thermal gradients and consequently result in an increased deviation in hardness. Figure 7b also shows that the in situ heat treatment is resulting in a strong decrease in hardness of ~ 200 HV0.1, due to tempering effects as discussed by Hearn et al. [32]. The impact of the original laser power is not visible anymore, while the tendency of increasing hardness by increasing exposure speed still appears to be visible, though not statistically significant anymore. The results show that even though a theoretical maximum hardness of around 620 HV0.1 is possible, the in situ heat treatment applied in subsequent layers will limit this maximum to approx. 500 HV0.1. The investigations above in Sect. “Flexibility of primary exposure

parameters” also show that the thermal load cannot be reduced by energy density or Δt_p without compromising the relative mass density. Alternative approaches to reduce the thermal load caused by the primary exposure could be adaptations in layer thickness or powder bed temperature.

Impact of secondary exposure parameters

The impact of the secondary exposure parameters is investigated based on the following primary exposure parameters: $P_p = 170$ W, $v_p = 880$ mm/s, $h_p = 0.08$ mm and $\Delta t_p \approx 1$ s.

Relative mass density

Figure 8 illustrates the impact of P_s and v_s onto the relative mass density. A negative impact resulting from h_s , Δt_s or exposure speeds above 600 mm/s is not expected and has not been investigated. Samples exposed to $v_s = 50$ and 100 mm/s result in a significant decrease in density.

The keyholing porosities causing this drop can be observed by LOM. The results regarding the keyholing phenomena show a mismatch with the theoretical, threshold-based, keyholing definition of $W/D < 1.5$. This could be due to several reasons: E.g., unsuitable

threshold value; exposure of powder vs. bulk material (see Sect. “Methodology for in situ heat treatment”); or keyholing effects are not sufficient to impact the measurements significantly.

Hardness

Figure 9 illustrates the impact of P_s and v_s under the two different conditions $\Delta t_s = \text{min.}$ and $\Delta t_s = 1$ s onto the hardness, while the secondary exposure is applied in every process layer ($l_s = l = 30$ μm). Regarding $\Delta t_s = \text{min.}$, a decreasing hardness of approx. 380 HV10, 390 HV10 can be observed at $v_s = 50$ mm/s and 100 mm/s, respectively. No significant effect can be identified for increased exposure speeds. This observation is in accordance with the assumption that an increased thermal load will result in tempering effects and therefore lower hardness. The $\Delta t_s = 1$ s state in contrast shows an increasing hardness with increasing exposure speed, as well as a turning point at 400 mm/s and approx. 490 HV10.

The reason for this turning point is noticeable in the LOM images presented in Fig. 10. While Fig. 10a ($P_s = 170$ W, $v_s = 400$ mm/s) is only showing laser tracks resulting from the secondary exposure (identified based on the single laser track experiments in Sect. “Expectations regarding Hardness based on Single

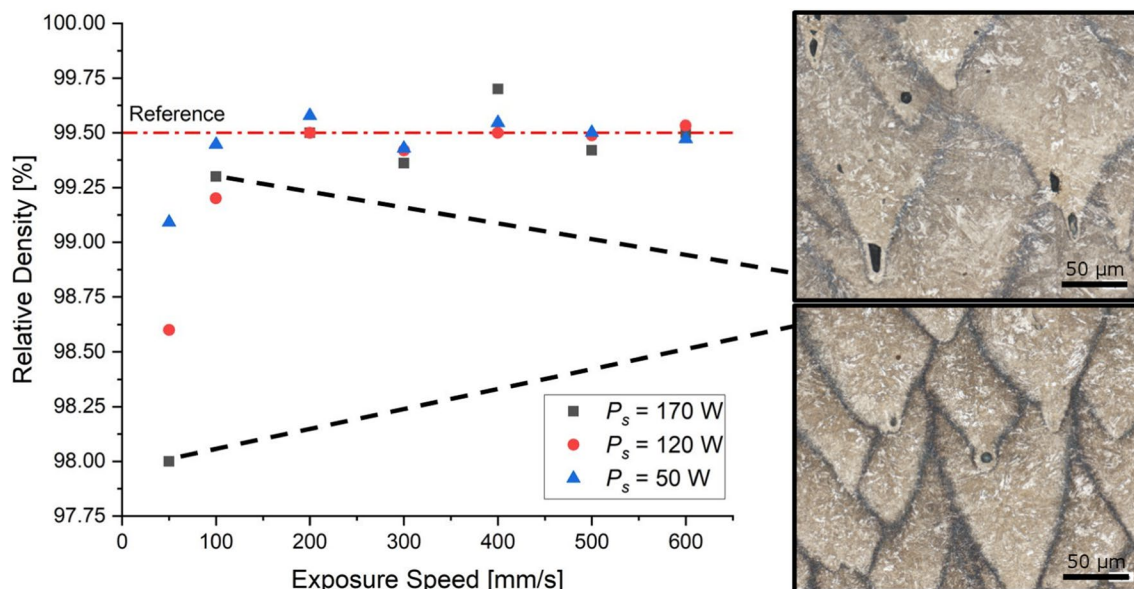


Figure 8 Relative mass densities resulting from changes in exposure speed (energy density) and hatch distance. Hatch distance is given relative to melt pool width (see cross section measurements in Figs. 3 and 7). LOM images on right hand side show porosities in melt pool tip resulting from keyholing phenomena. $h_s = 50\%$, $\Delta t_s = 1$ s, $l_s = 30$ μm .

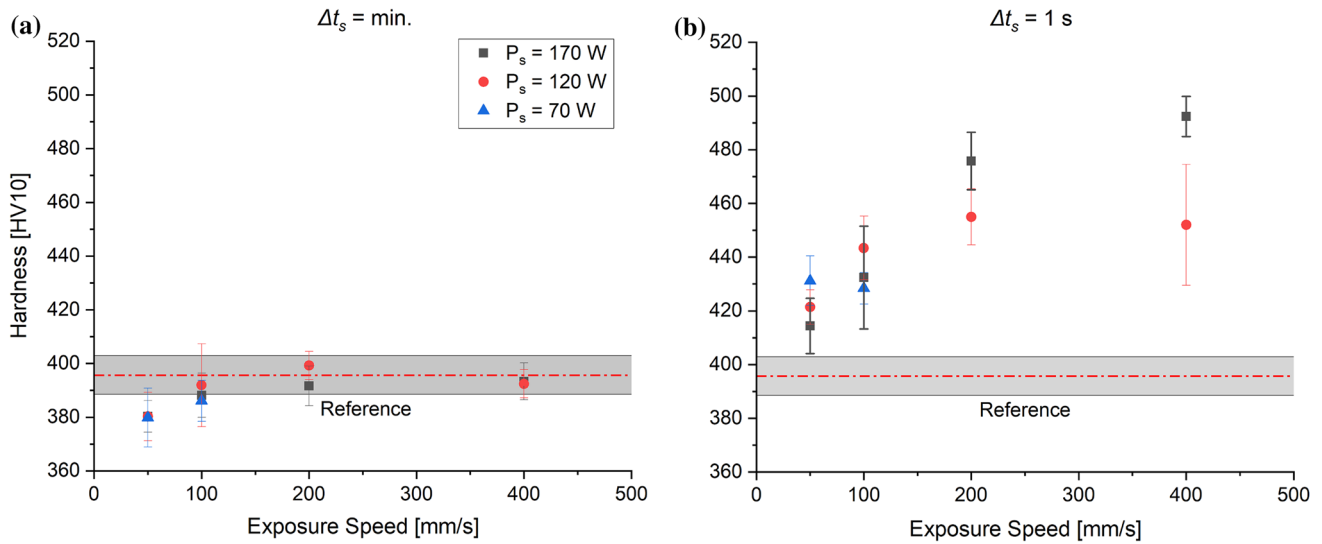


Figure 9 Impact of P_s and v_s on hardness at a hatch distance of 50% relative to melt pool width and layer thickness $l_s = 30 \mu\text{m}$. Measurement method: Macro-hardness. **a** $\Delta t_s = \text{min.}$ state enables softer microstructures; **b** $\Delta t_s = 1 \text{ s}$ state enables harder microstructures.

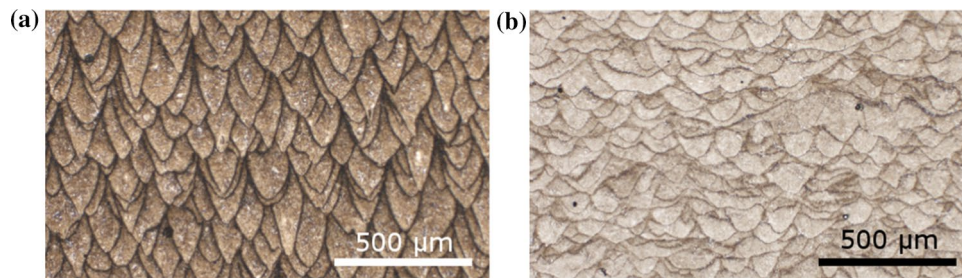


Figure 10 Optical micrographs of samples manufactured under the following secondary exposure parameters: **a** Only secondary exposure tracks are visible. $P_s = 170 \text{ W}$, $v_s = 400 \text{ mm/s}$, $h_s = 50\%$,

$l_s = 30 \mu\text{m}$; **b** Primary and secondary exposure tracks are not clearly distinguishable. $P_s = 170 \text{ W}$, $v_s = 600 \text{ mm/s}$, $h_s = 50\%$, $l_s = 30 \mu\text{m}$.

Laser Track Experiments”), the laser tracks in Fig. 10b ($P_s = 170 \text{ W}$, $v_s = 600 \text{ mm/s}$) cannot be clearly associated with primary or secondary exposure. It is therefore concluded that the penetration depths of secondary and primary exposure start to overlap, resulting in a mix of measured secondary and primary exposure tracks, since the hardness indent covers several laser tracks (size $\sim 200 \mu\text{m}$). This also explains the increased standard deviation for these samples. The results are in accordance with the assumption that an increased thermal load will result in increased tempering effects and therefore in a lower hardness, while secondary exposure parameters, which are re-melting deeper areas, will be subject to lower thermal load and thus result in an increased hardness. Also, the impact caused by the intensity of the thermal load is visible in

the results. An increased exposure speed is therefore resulting in higher hardness.

The impact of the secondary layer thickness l_s is analyzed in Fig. 11. In general, the results show that an increasing l_s will increase the resulting hardness. Looking closer at the results, a trend of increasing standard deviation with increasing secondary layer thickness l_s can be observed, especially for $\Delta t_s = \text{min.}$ This assumedly represents an increasing gradation of the material. Since with an increasing secondary layer thickness l_s , the secondary laser tracks re-melt smaller amounts of the former secondary laser tracks, the melt pool residuals experience an increasing temperature profile resulting in an increasing gradation of the laser tracks in the final microstructure. Furthermore, a second effect can be observed in Fig. 11. The

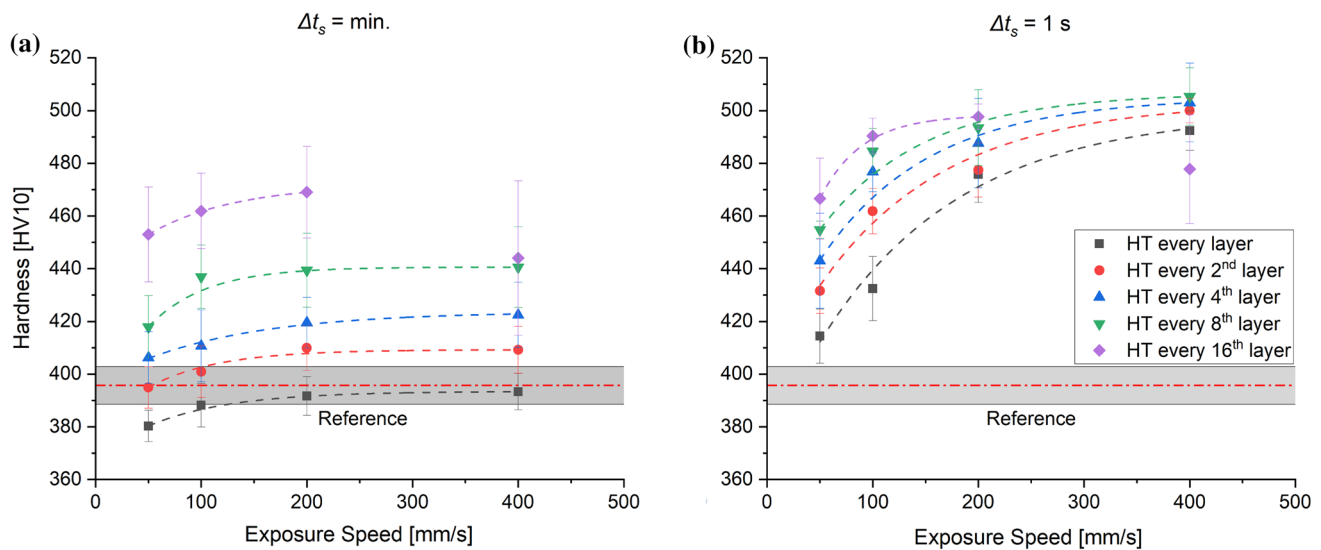


Figure 11 Impact of layer-wise application of secondary exposure. Measurement method: Macro-hardness. HT = in situ heat treatment/secondary exposure. $P_s = 170 \text{ W}$, $h_s = 50\%$, $l_s = 30 \mu\text{m}$. **a** $\Delta t_s = \text{min.}$; **b** $\Delta t_s = 1 \text{ s.}$

samples at $v_s = 400 \text{ mm/s}$ and $l_s = 16\text{th}$ layer show a sudden drop in hardness combined with the highest observed standard deviations. When looking at the penetration depths (see Fig. 3b) of the applied exposure parameters, it becomes clear that the depth of the secondary laser tracks is close to the secondary layer thickness l_s . LOM reveals laser track residuals of different sizes. Thus, the resulting material presents a mix of secondary and primary laser track. The microstructure is therefore already presenting a layer-wise FGMi. Measuring the different areas of this material are resulting in a distorted mean and standard deviation of the sample.

Proof of Hypothesis 2 The results regarding the hardness (Fig. 11) in combination with the results regarding the relative mass density (Fig. 8) show in contrast to the results regarding the flexibility of primary exposure parameters in Sect. “Flexibility of primary exposure parameters” that a wide spectrum of in situ heat treatments resulting in microstructural changes can be applied without compromising the relative mass density, due to the presented double exposure approach.

Proof of Hypothesis 3 The results in Fig. 11b proof that the introduction of cooling phases between single exposure tracks facilitate the highest increase in hardness.

Figure 12 presents the impact of the secondary hatch distance h_s onto the hardness. The results show a decreasing hardness with increasing hatch distance. OM images reveal the same effect as shown in Fig. 10. The microhardness starts to be dominated by primary laser tracks, since the increasing hatch distance is causing gaps between the secondary exposure tracks. A decreasing hatch distance in contrast results in a larger overlap of laser track. The resulting microstructures are therefore dominated by residuals of the outer melt pool areas, while inner melt pool areas are re-melted. As mentioned above, a tendency of a softer core and harder hardness values toward the edges of melt pools has been observed. EBSD measurements as illustrated within Fig. 13 reveal smaller grain sizes within the outer melt pool residuals, but especially a significantly lower image quality (IQ) as well as kernel average misorientation (KAM). The observed increasing hardness by decreasing hatch could therefore be explained by different effects, such as smaller grain size as observed by IPF mapping, lattice distortions based on the KAM mapping or lattice imperfections based on the IQ mapping. Additionally, to the findings above, the impact of additional break time between single process layers as presented by Kürsteiner et al. [23] was tested without any significant impact onto the hardness.

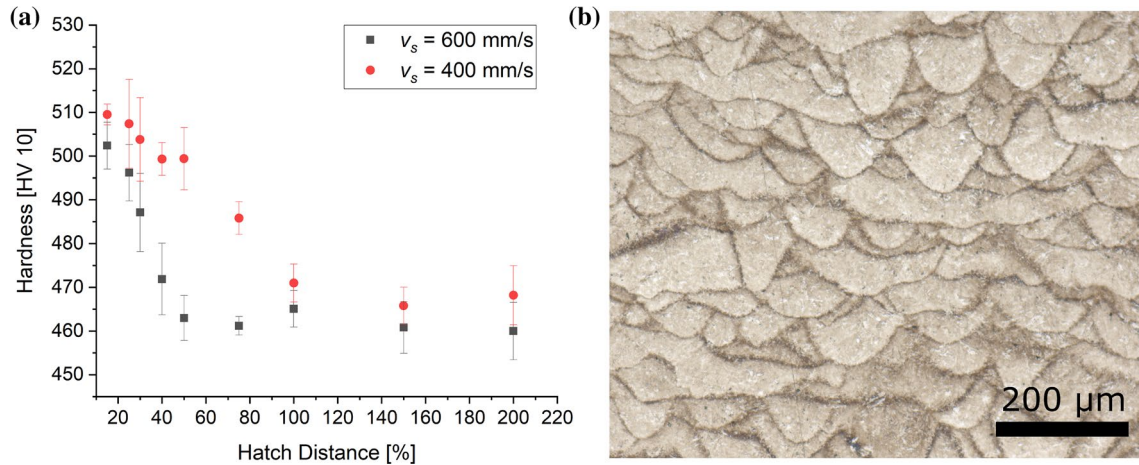


Figure 12 **a** Impact of hatch distance h_s on hardness. Hatch distance is given relative to melt pool width. $P_s=170$ W, $\Delta t_s=1$ s, $l_s=60$ μm ; **b** The microstructure of the material generated by

the following parameter is showing gaps between the secondary exposure tracks resulting in a decreasing hardness. $P_s=170$ W, $v_s=600$ mm/s, $h_s=100\%$, $\Delta t_s=1$ s, $l_s=60$ μm .

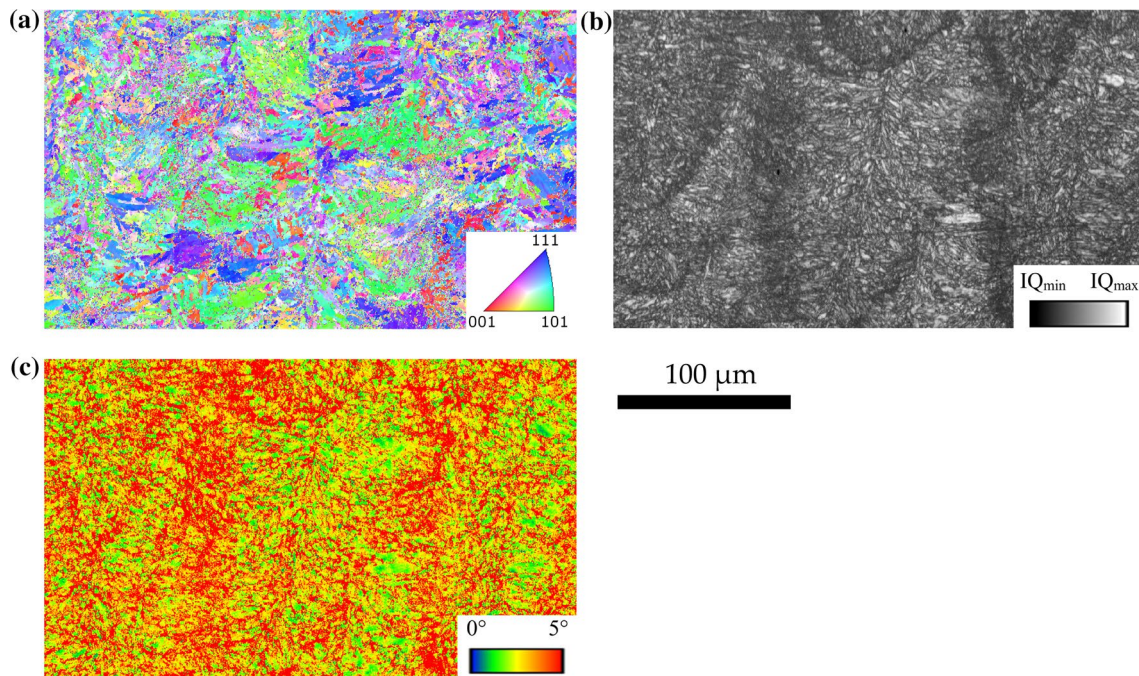


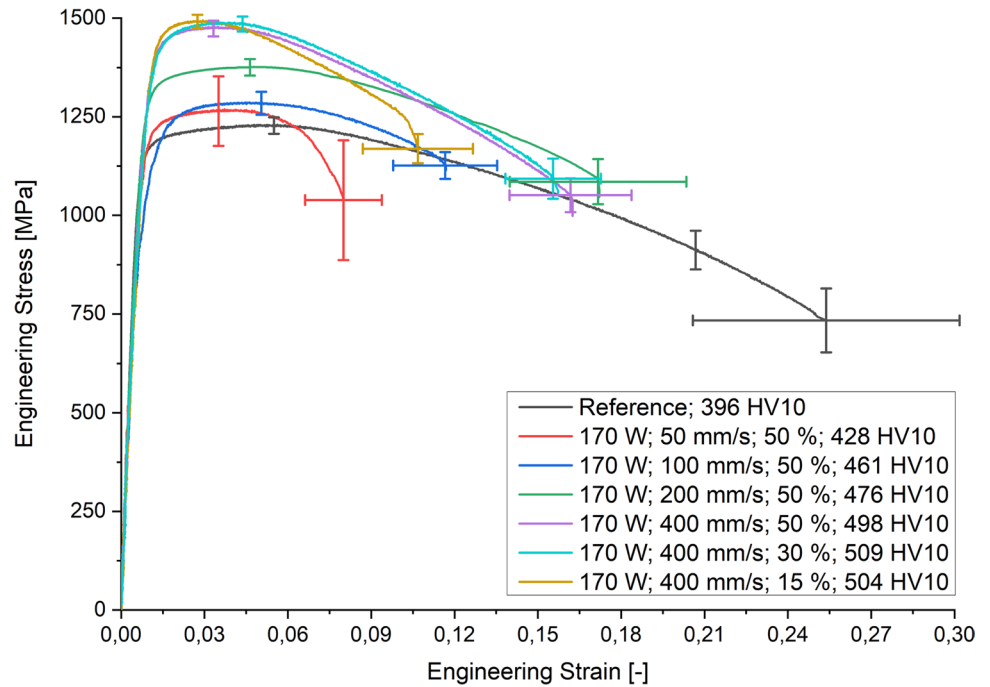
Figure 13 EBSD measurement on sample $P_s=170$ W, $v_s=400$ mm/s, $h_s=50\%$, $\Delta t_s=1$ s, $l_s=60$ μm **a** IFP mapping. **b** IQ mapping. **c** KAM mapping (3rd neighbor; angle restriction 5°).

Influencing tensile properties by in situ heat treatment

The most promising parameter combinations are tested on their monotonic tensile properties. All samples were manufactured within one print and tested in z-direction (build direction) in an “as-built” surface

state. Figure 14 presents representative stress–strain curves for each material state. The results show a significant increase in ultimate tensile strength (UTS) by approx. 21.3% in combination with a decreasing elongation at break by approx. 35% for the hardest sample compared to the none in situ heat treated reference sample. However, softer in situ heat treated

Figure 14 Stress–Strain curves resulting from different secondary exposure parameters. Notation within legend: P_s , v_s , h_s , achieved hardness. Deviations based on three valid tests. $l_s = 30 \mu\text{m}$. $\Delta t_s = 1 \text{ s}$.



samples do not show an improved ductility compared to harder samples as could be expected. This could be due to porosities resulting from keyholing effects (see

Figs. 8). A linear correlation between hardness and UTS can be observed, resulting in a hardness-UTS factor of 2.91 ($\sigma = 0.09$). Hardness measurements were

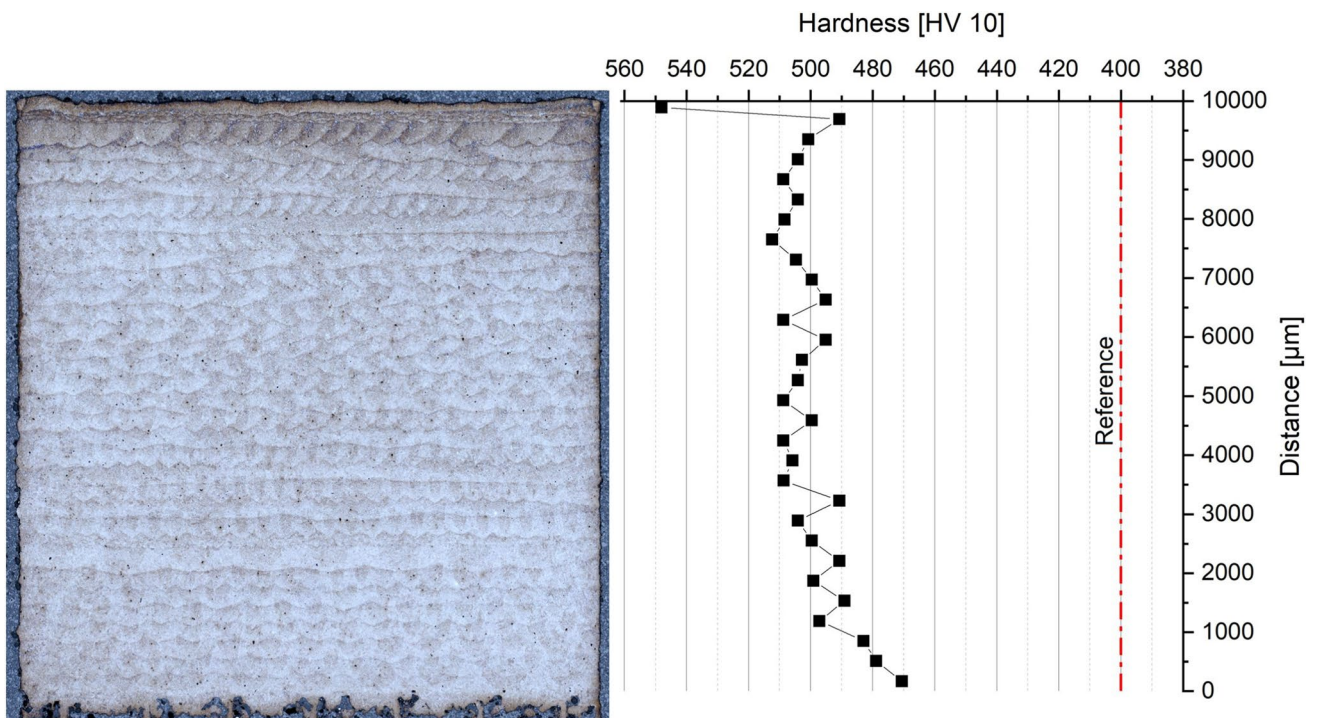


Figure 15 Homogeneously in situ heat treated $10 \times 10 \times 10 \text{ mm}$ cube. Secondary exposure parameters: $P_s = 170 \text{ W}$, $v_s = 400 \text{ mm/s}$, $h_s = 50\%$, $\Delta t = 1 \text{ s}$, $l_s = 30 \mu\text{m}$.

carried out directly on tensile specimens. The demonstrated changes in strength, hardness and ductility offer the change to tailor the mechanical properties of components for different load scenarios. E.g.: Simulations of lattice structures under high strain loads (e.g., see Imbalzano et al. [6]) show that the plastic deformation is resulting in localized plastic deformation within the lattice cell. Areas of higher plastic deformation would require a more ductile material, while other areas require a higher strength for an optimized energy absorption.

Generating functionally graded microstructures

The findings can be used to apply a homogeneous, graded or discrete in situ heat treatment to a part in order to adapt its mechanical properties. Figure 15 shows a homogeneous in situ heat treated microstructures, which could be used to tailor the strength-ductility trade-off for a given application scenario. The example also shows the limitation of a homogeneous application. The first process layers (downskin area) of the part exhibit a significantly lower hardness (~ 480 HV10 instead of ~ 500 HV10). This is assumed to be the result of heat accumulation due to the use of

filigree support structures below the sample, resulting in an reduced thermal conductivity. Such areas are subject to increased thermal loads resulting in increased tempering effects. Furthermore, the last process layer is not experiencing any heat treatment resulting in an increased hardness (~ 550 HV10 instead of ~ 500 HV10). This layer will not be measured in the following two examples.

Figure 16 presents a continuously graded FGMi, realized by the following secondary exposure parameters: $P_s = 170 \text{ W}$, $v_s = 50 \text{ mm/s}$, $h_s = 180\%$, $\Delta t = \text{min}$. In order to grade the sample, the secondary exposure is not applied in every layer. Instead, the application is continuously increased by one layer thickness, i.e., the distance between the first and second double exposure is one layer thickness l , between second and third $2l$

Table 1 Secondary exposure parameters used within different sections of the sample in Fig. 17

	0 to 2.5 mm	2.50 to 5 mm	5 to 7.5 mm	7.5 to 10 mm
P_s	-	170 W	170 W	170 W
v_s	-	400 mm/s	200 mm/s	100 mm/s
h_s	-	50%	50%	50%
l_s	-	0.3 mm	0.36 mm	0.54 mm

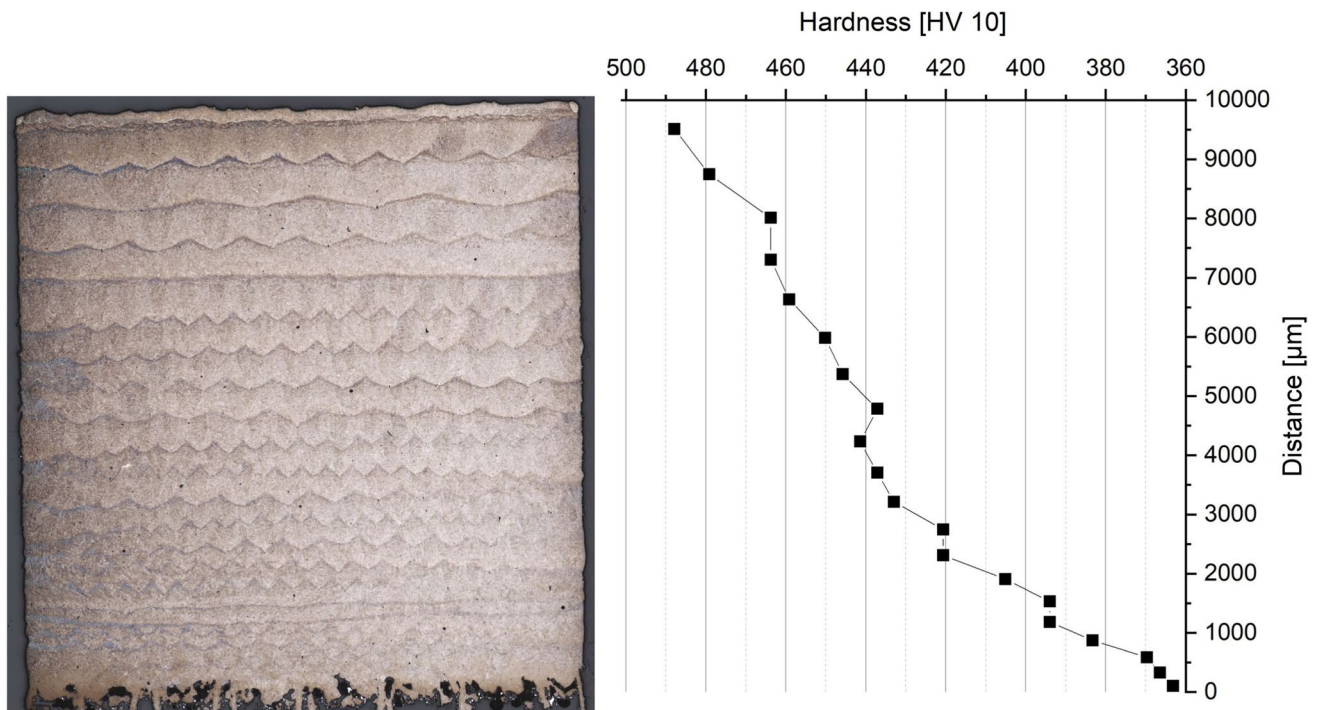


Figure 16 Demonstration of a continuously graded microstructures. In Situ heat treated by the following secondary exposure parameters: $P_s = 170 \text{ W}$, $v_s = 50 \text{ mm/s}$, $h_s = 180\%$, $\Delta t = \text{min}$, $l_s = l_{s-1} + l_p$

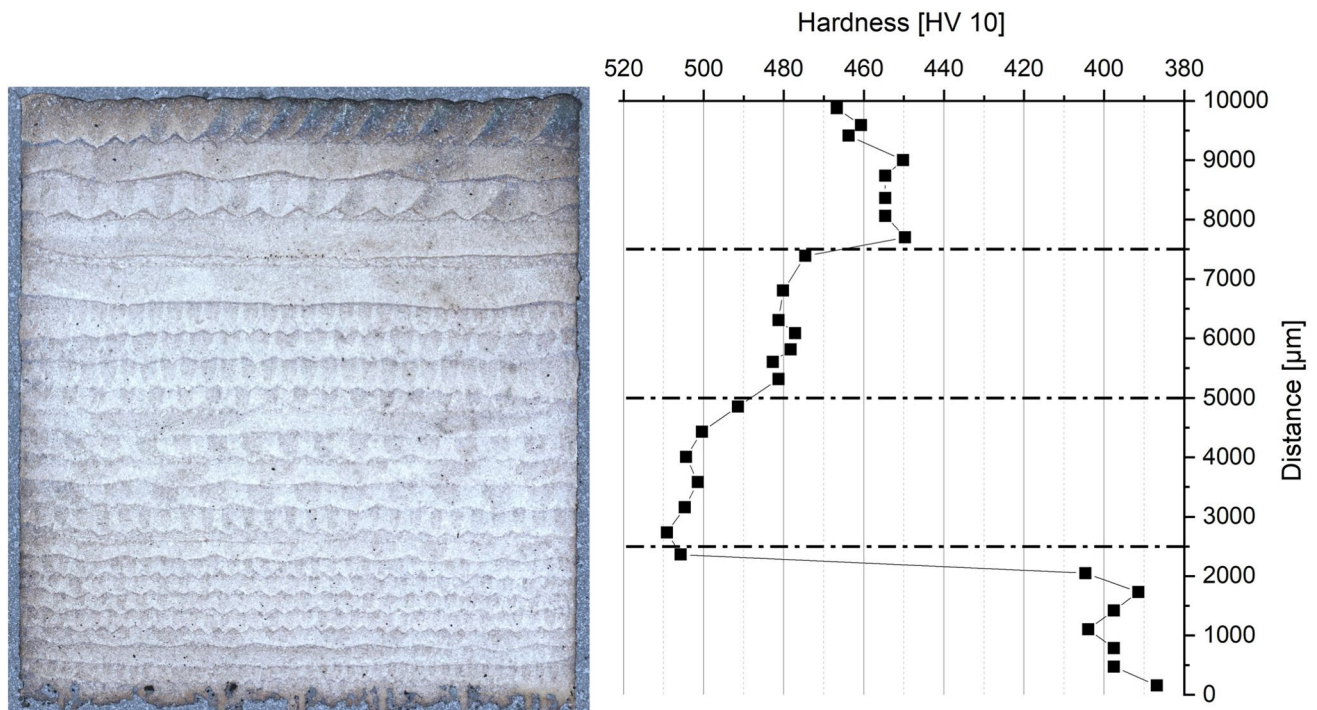


Figure 17 Demonstration of a discrete graded microstructures. In situ heat treated by the secondary exposure parameters listed in table 1. $\Delta t = 1$ s.

and between third and fourth $3 l$. This approach results in a high thermal load in lower areas and a reduced thermal load as well as deeper re-melted and therefore less in situ heat treated areas with increasing built height. The hardness curve shows a steady increase from the lower edge of the component with a hardness of 363 HV10 to the upper edge with 489 HV10. The value of 363 HV10 in the lower areas of the sample is lower than anticipated by the results above. This can be explained by the same downskin-effect as in Fig. 15. Graded microstructures will enable combination of material properties within a single part. Hardness gradients can offer advantages in cutting tools, bearings, gears, tool dies or protection against penetrators.

Regarding the discrete FGMi, the sample is divided into four equal areas, each 0.25 mm high. The choice of parameters for each section is given in Table 1. Figure 17 shows the microsection of the sample and the associated hardness profile. The result shows a good separation of the different sections. However, the lowest values within Sect. “Materials and methods” and “Results and discussions” seem to be impacted by the thermal load caused by the parameters of the following section.

Microstructural analysis

Looking at the literature (e.g., see [50, 65–70]), it is clear that single laser tracks result in an extremely high cooling rate, which necessarily leads to martensitic microstructures. However, it is also known that the continuous application of several laser tracks, as it is the case for actual three-dimensional parts, results in an increasing part temperature, as shown by Chelonie et al. [50], Chae et al. [69] and Promopattum et al. [67]. Own measurements by pyrometry (measurement setup see Pfaff et al. [66]) concerning the investigated alloy show that the exposure of a part can take several seconds and increases the part’s temperature by several hundred degrees which could theoretically lead to bainitic phases. LOM images reveal needle-like or lath-shaped morphologies, which according to Oettel [71] can be interpreted as martensitic. It is therefore assumed that the investigated microstructures are martensitic and the variations in hardness present different states of tempered martensite. When analyzing the continuously graded microstructures (see Fig. 18), a high amount of presumed martensite can be observed within the last process layer which did

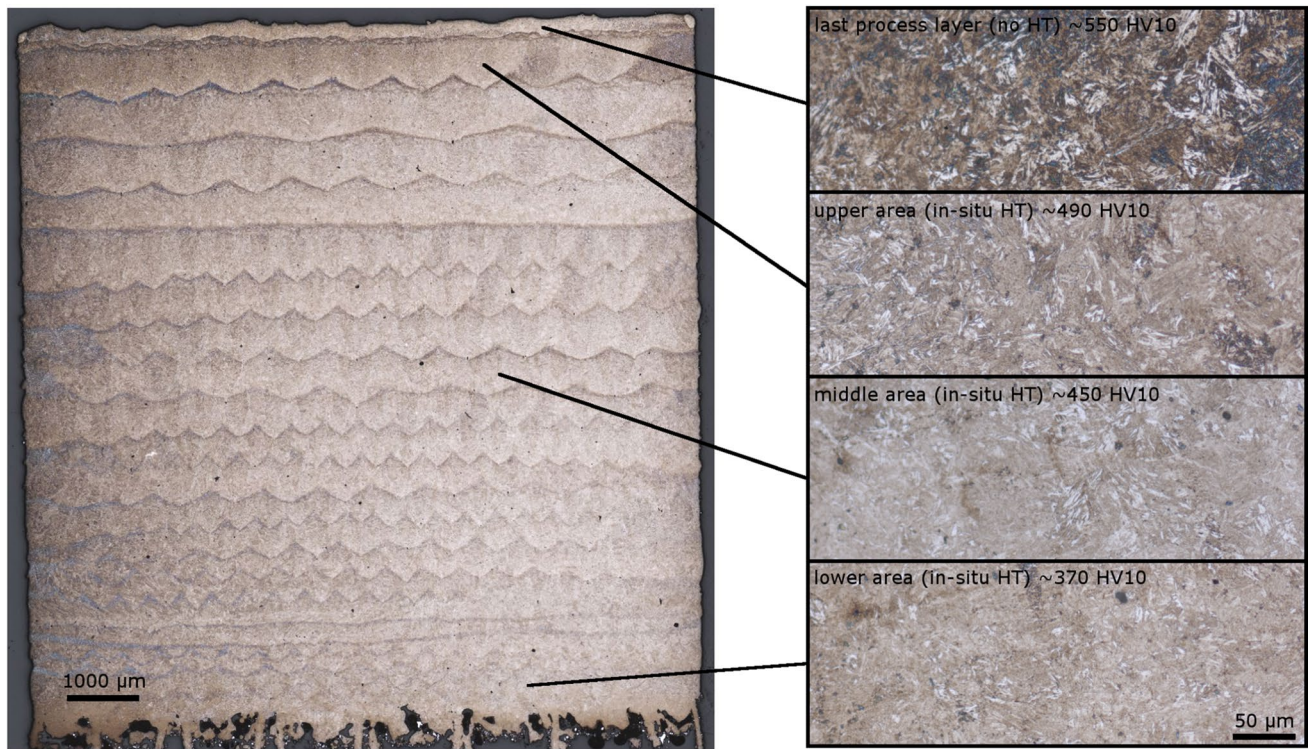


Figure 18 LOM analysis of nital-etched continuously graded hardness specimen (see Fig. 16).

not receive any in situ heat treatment. Laser tracks directly below but still in the upper area received an in situ heat treatment and show a strong decrease in presumed lath-martensite. Middle and lower areas, which received increasing thermal loads due to the parameter selection, show increased tempering effects. A constant decrease in needle-like morphologies and needle size can be observed.

Conclusions

The presented double exposure approach within this work is enabling in situ heat treatments in order to create FGMi by L-PBF. The primary exposure ensures a high relative mass density, while the secondary exposure serves as a variable for the in situ heat treatment. Changes in microstructures are measured indirectly by hardness measurements. This is done based on the correlation of microstructures, hardness and resulting mechanical tensile properties. The presented approach is tested for the low-alloy steel 30CrMoNb5-2, providing the following findings for this alloy:

- Increased parameter flexibility**
 The results show that in contrast to a single exposure strategy, the double exposure approach enables process parameter variations leading to microstructures of different mechanical properties, without compromising the relative mass density.
- Correlating process parameter changes and resulting hardness**
 The impact of the secondary exposure parameters laser power, exposure speed, hatch distance, cooling time between laser tracks and layer thickness is investigated. The results enable a hardness spectrum of approx. 380–510 HV10 for the investigated alloy. Harder and softer areas between approx. 360–620 HV can be realized in the final and first layers.
- Resulting tensile properties**
 Tensile tests show an increase in UTS by approx. 21.3%, in combination with a reduction in the elongation at break by approx. 35% when comparing the hardest sample with a non-intentional in situ heat treated sample (single exposure).

- **Demonstrating FGM**

Three types of FGMi are realized and serve as demonstrators for the proposed strategy. Homogeneously applied in situ heat treatments can serve to adapt the mechanical properties of a material. A continuously graded sample demonstrates a linear hardness gradient between 363 and 489 HV10. Further, a discrete change in hardness demonstrates the possibility to create areas of different microstructures side by side.

Within this work, the microstructural changes are identified by hardness measurements, since the microstructural analysis are time consuming, intricate in interpretation and prone to errors due to the expectable phases which are all based on body-centered crystal structure (e.g., martensite, bainite, ferrite). To enable a better understanding of the generated microstructures, future works can focus on the microstructural analysis (e.g., based on SEM-EBSD). Furthermore, the results show that the microstructure is not only a result of the cooling duration but also of the heat treatment resulting from subsequent layers. Therefore, measurements regarding the thermal load resulting from different parameter conditions and the corresponding microstructural changes in Z (build) and XY direction are of high relevance in order to create target orientated FGMi. Such a knowledge could also support the development of primary process parameters resulting in a lower thermal load.

Additional remark regarding Δt_p

Within this work, the break times between each laser track Δt_p are set to 1 s in order to ensure significant cool down of the part. This value is rather arbitrary and not optimized so far, causing a strong increase in manufacturing time. First own measurements (see Pfaff et al. [66]) suggest that it could be reduced to a few milliseconds. Furthermore, randomized scanning strategy as demonstrated by Zrodowski [72] offers additional potential to reduce the manufacturing time.

Data and code availability

Additional data will be made available upon request.

Acknowledgements

This work was supported by the Bundeswehr Research Institute for Materials Fuels and Lubricants (WIWeB), Erding, Germany [grant number E/E210/AK030/GF126].

Author contribution

AP was contributed to conceptualization, methodology, validation, formal analysis, investigation, resources, data curation, writing—original draft, writing—review and editing, visualization, project administration, funding acquisition. ML was contributed to investigation, visualization, writing—review and editing. KH was contributed to resources, writing—review and editing, funding acquisition. FB was contributed to writing—review and editing, supervision.

Funding

Open Access funding enabled and organized by Projekt DEAL.

Declarations

Conflict of interest The authors declare that they have no known conflict of interest or competing financial interests or personal relationships that could have appeared to influence the work reported in this paper.

Open Access This article is licensed under a Creative Commons Attribution 4.0 International License, which permits use, sharing, adaptation, distribution and reproduction in any medium or format, as long as you give appropriate credit to the original author(s) and the source, provide a link to the Creative Commons licence, and indicate if changes were made. The images or other third party material in this article are included in the article's Creative Commons licence, unless indicated otherwise in a credit line to the material. If material is not included in the article's Creative Commons licence and your intended use is not permitted by statutory regulation or exceeds the permitted use, you will need to obtain permission directly from the copyright holder. To view a copy of

this licence, visit <http://creativecommons.org/licenses/by/4.0/>.

References

- [1] Miyamoto Y, Kaysser WA, Rabin BH, Kawasaki A, Ford RG (eds) (1999) Functionally graded materials: design, processing and applications. Materials technology series 5. Springer US, Boston
- [2] Mahamood RM (2017) Functionally graded materials. Topics in mining, metallurgy and materials engineering ser. Springer International Publishing AG, Cham
- [3] Pandey PM (ed) (2022) Functionally graded materials (FGMs): fabrication, properties, applications, and advancements. CRC Press, Boca Raton
- [4] Estrin Y, Bréchet Y, Dunlop J, Fratzl P (2019) Architected materials in nature and engineering 282. Springer International Publishing, Cham
- [5] Xiao L, Song W (2018) Additively-manufactured functionally graded Ti–6Al–4V lattice structures with high strength under static and dynamic loading: experiments. *Int J Impact Eng.* <https://doi.org/10.1016/j.ijimpeng.2017.09.018>
- [6] Imbalzano G, Tran P, Ngo TD, Lee PVS (2016) Three-dimensional modelling of auxetic sandwich panels for localised impact resistance. *J Sandwich Struct Mater.* <https://doi.org/10.1177/1099636215618539>
- [7] Ma GW, Ye ZQ (2007) Energy absorption of double-layer foam cladding for blast alleviation. *Int J Impact Eng.* <https://doi.org/10.1016/j.ijimpeng.2005.07.012>
- [8] Harris JA, Winter RE, McShane GJ (2017) Impact response of additively manufactured metallic hybrid lattice materials. *Int J Impact Eng.* <https://doi.org/10.1016/j.ijimpeng.2017.02.007>
- [9] Conrads L, Liebsch C, Hirt G (2017) Increasing the energy absorption capacity of structural components made of low alloy steel by combining strain hardening and local heat treatment. *Proc Eng.* <https://doi.org/10.1016/j.proeng.2017.10.771>
- [10] Bambach M, Conrads L, Daamen M, Güvenç O, Hirt G (2016) Enhancing the crashworthiness of high-manganese steel by strain-hardening engineering, and tailored folding by local heat-treatment. *Mater Des.* <https://doi.org/10.1016/j.matdes.2016.07.065>
- [11] Conrads L, Daamen M, Hirt G, Bambach M (2016) Improving the crash behavior of structural components made of advanced high strength steel by local heat treatment. *IOP Conf Ser Mater Sci Eng.* <https://doi.org/10.1088/1757-899X/159/1/012024>
- [12] Masood SH, Ruan D, Rajapatruni P (2018) Mechanical performance of plymetal structures subjected to impact loading. *Int J Protect Struct.* <https://doi.org/10.1177/2041419617729380>
- [13] Simoes M, Harris JA, Ghose S, Hooper PA, McShane GJ (2022) Process parameter sensitivity of the energy absorbing properties of additively manufactured metallic cellular materials. *Mater Des.* <https://doi.org/10.1016/j.matdes.2022.111398>
- [14] Pfaff A, Jäcklein M, Hoschke K, Wickert M (2018) Designed materials by additive manufacturing—impact of exposure strategies and parameters on material characteristics of AlSi10Mg processed by laser beam melting. *Metals.* <https://doi.org/10.3390/met8070491>
- [15] Kieback B, Neubrand A, Riedel H (2003) Processing techniques for functionally graded materials. *Mater Sci Eng A.* [https://doi.org/10.1016/S0921-5093\(03\)00578-1](https://doi.org/10.1016/S0921-5093(03)00578-1)
- [16] Mahamood RM, Akinlabi Member ET, IAENG, Shukla M, Pityana S (2012) Functionally graded material: an overview: the 2012 international conference of manufacturing engineering and engineering management, the 2012 international conference of mechanical engineering. Lecture notes in engineering and computer science Vol. 3. IAENG, Hong Kong
- [17] Karabulut Y, Ünal R (2022) Additive manufacturing of ceramic particle-reinforced aluminum-based metal matrix composites: a review. *J Mater Sci.* <https://doi.org/10.1007/s10853-022-07850-0>
- [18] Gebhardt A (2013) Generative fertigungsverfahren: additive manufacturing und 3D drucken für prototyping; tooling; produktion, 1st edn. Carl Hanser Fachbuchverlag, s.l.
- [19] Wohlers T, Campbell RI, Diegel O, Kowen J, Mostow N, Fidan I (2022) Wohlers report 2022: 3D printing and additive manufacturing global state of the industry. Wohlers Associates; ASTM International, Fort Collins, Colo., Washington, DC
- [20] Spears TG, Gold SA (2016) In-process sensing in selective laser melting (SLM) additive manufacturing. *Integr Mater Manuf Innov.* <https://doi.org/10.1186/s40192-016-0045-4>
- [21] Yadroitsev I (2009) Selective laser melting: direct manufacturing of 3D-objects by selective laser melting of metal powders. LAP Lambert Academic Publ, Saarbrücken
- [22] Fayazfar H, Salarian M, Rogalsky A, Sarker D, Russo P, Paserin V, Toyserkani E (2018) A critical review of powder-based additive manufacturing of ferrous alloys: process parameters, microstructure and mechanical properties. *Mater Des.* <https://doi.org/10.1016/j.matdes.2018.02.018>

- [23] Kürnsteiner P, Wilms MB, Weisheit A, Gault B, Jäggle EA, Raabe D (2020) High-strength Damascus steel by additive manufacturing. *Nature*. <https://doi.org/10.1038/s41586-020-2409-3>
- [24] Freeman FS, Lincoln A, Sharp J, Lambourne A, Todd I (2019) Exploiting thermal strain to achieve an in-situ magnetically graded material. *Mater Des*. <https://doi.org/10.1016/j.matdes.2018.11.011>
- [25] Freeman FS, Sharp J, Xi J, Todd I (2019) Influence of solidification cell structure on the martensitic transformation in additively manufactured steels. *Addit Manuf*. <https://doi.org/10.1016/j.addma.2019.100917>
- [26] Zrodowski, Lukasz, Rafał Wróblewski, Marcin Leonowicz, Bartosz Morończyk, et al. How to control the crystallization of metallic glasses during laser powder bed fusion? Towards part-specific 3D printing of in situ composites. Sydney NSW 2022 Australia 2022
- [27] Popovich VA, Borisov EV, Sufiyarov VS, Popovich AA (2019) Tailoring the properties in functionally graded alloy inconel 718 using additive technologies. *Met Sci Heat Treat*. <https://doi.org/10.1007/s11041-019-00343-z>
- [28] Popovich VA, Borisov EV, Popovich AA, Sufiyarov V, Masaylo DV, Alzina L (2017) Functionally graded Inconel 718 processed by additive manufacturing: Crystallographic texture, anisotropy of microstructure and mechanical properties. *Mater Des*. <https://doi.org/10.1016/j.matdes.2016.10.075>
- [29] Nematollahi M, Safaei K, Bayati P, Elahinia M (2021) Functionally graded NiTi shape memory alloy: selective laser melting fabrication and multi-scale characterization. *Mater Lett*. <https://doi.org/10.1016/j.matlet.2021.129648>
- [30] Donik Č, Kraner J, Paulin I, Godec M (2020) Influence of the energy density for selective laser melting on the microstructure and mechanical properties of stainless steel. *Metals*. <https://doi.org/10.3390/met10070919>
- [31] Niendorf T, Brenne F, Krooß P, Vollmer M, Günther J, Schwarze D, Biermann H (2016) Microstructural evolution and functional properties of fe-mn-al-ni shape memory alloy processed by selective laser melting. *Metall Mat Trans A*. <https://doi.org/10.1007/s11661-016-3412-z>
- [32] Hearn W, Lindgren K, Persson J, Hryha E (2022) In situ tempering of martensite during laser powder bed fusion of Fe-0.45C steel. *Materialia*. <https://doi.org/10.1016/j.mtla.2022.101459>
- [33] Yasa E, Kruth J-P (2011) Microstructural investigation of selective laser melting 316L stainless steel parts exposed to laser re-melting. *Proc Eng*. <https://doi.org/10.1016/j.proeng.2011.11.130>
- [34] Yasa E, Deckers J, Kruth J-P (2011) The investigation of the influence of laser re-melting on density, surface quality and microstructure of selective laser melting parts. *Rapid Prototyp J*. <https://doi.org/10.1108/13552541111156450>
- [35] Xie JW, Fox P, O'Neill W, Sutcliffe CJ (2005) Effect of direct laser re-melting processing parameters and scanning strategies on the densification of tool steels. *J Mater Process Technol*. <https://doi.org/10.1016/j.jmatprotec.2005.05.055>
- [36] Siddique S, Imran M, Rauer M, Kaloudis M, Wycisk E, Emmelmann C, Walther F (2015) Computed tomography for characterization of fatigue performance of selective laser melted parts. *Mater Des*. <https://doi.org/10.1016/j.matdes.2015.06.063>
- [37] Huber F, Rasch M, Schmidt M (2021) Laser powder bed fusion (PBF-LB/M) process strategies for in-situ alloy formation with high-melting elements. *Metals*. <https://doi.org/10.3390/met11020336>
- [38] Huang S, Yeong WY (2018) Laser re-scanning strategy in selective laser melting for part quality enhancement: a review. Nanyang technological university
- [39] Onal E, Medvedev AE, Leeftang MA, Molotnikov A, Zadpoor AA (2019) Novel microstructural features of selective laser melted lattice struts fabricated with single point exposure scanning. *Addit Manuf*. <https://doi.org/10.1016/j.addma.2019.100785>
- [40] AlMangour B, Grzesiak D, Yang J-M (2017) Scanning strategies for texture and anisotropy tailoring during selective laser melting of TiC/316L stainless steel nanocomposites. *J Alloy Compd*. <https://doi.org/10.1016/j.jallcom.2017.08.022>
- [41] Zhan J, Wu J, Ma R, Li K, Lin J, Murr LE (2023) Tuning the functional properties by laser powder bed fusion with partitioned repetitive laser scanning: toward editable 4D printing of NiTi alloys. *J Manuf Process*. <https://doi.org/10.1016/j.jmapro.2023.07.009>
- [42] Zhang M, Sun C-N, Zhang X, Goh PC, Wei J, Hardacre D, Li H (2017) Fatigue and fracture behaviour of laser powder bed fusion stainless steel 316L: influence of processing parameters. *Mater Sci Eng A*. <https://doi.org/10.1016/j.msea.2017.07.071>
- [43] Kumar P, Farah J, Akram J, Teng C, Ginn J, Misra M (2019) Influence of laser processing parameters on porosity in inconel 718 during additive manufacturing. *Int J Adv Manuf Technol*. <https://doi.org/10.1007/s00170-019-03655-9>
- [44] Kan WH, Chiu LNS, Lim CVS, Zhu Y, Tian Y, Jiang D, Huang A (2022) A critical review on the effects of process-induced porosity on the mechanical properties of alloys fabricated by laser powder bed fusion. *J Mater Sci*. <https://doi.org/10.1007/s10853-022-06990-7>

- [45] Calignano F, Minetola P (2019) Influence of process parameters on the porosity, accuracy, roughness, and support structures of Hastelloy X produced by laser powder bed fusion. *Materials*. <https://doi.org/10.3390/ma12193178>
- [46] Pfaff A, Jäcklein M, Schlager M, Harwick W, Hoschke K, Balle F (2020) An empirical approach for the development of process parameters for laser powder bed fusion. *Materials*. <https://doi.org/10.3390/ma13235400>
- [47] Yadroitsev I, Yadroitsava I (2021) In: *Fundamentals of laser powder bed fusion of metals*. Elsevier, pp 39–77
- [48] Fraunhofer Direct Digital Manufacturing Conference, Fraunhofer-Allianz Generative Fertigung, DDMC (2018) LBM process parameter optimization for designed materials: fraunhofer direct digital manufacturing conference proceedings direct digital manufacturing conference, Berlin, March 14–15, 2018. Fraunhofer Verlag, Stuttgart
- [49] Haghdadi N, Laleh M, Moyle M, Primig S (2021) Additive manufacturing of steels: a review of achievements and challenges. *J Mater Sci*. <https://doi.org/10.1007/s10853-020-05109-0>
- [50] Cheloni JP, Fonseca EB, Gabriel AH, Lopes ÉS (2022) The transient temperature field and microstructural evolution of additively manufactured AISI H13 steel supported by finite element analysis. *J Market Res*. <https://doi.org/10.1016/j.jmrt.2022.06.143>
- [51] Madison JD, Aagesen LK (2012) Quantitative characterization of porosity in laser welds of stainless steel. *Scripta Mater*. <https://doi.org/10.1016/j.scriptamat.2012.06.015>
- [52] Johnson L, Mahmoudi M, Zhang B, Seede R, Huang X, Maier JT, Maier HJ, Karaman I, Elwany A, Arróyave R (2019) Assessing printability maps in additive manufacturing of metal alloys. *Acta Mater*. <https://doi.org/10.1016/j.actamat.2019.07.005>
- [53] Pal S, Gubeljak N, Bončina T, Hudák R, Toth T, Zivcak J, Lojen G, Leben N, Drstvenšek I (2021) The effects of locations on the build tray on the quality of specimens in powder bed additive manufacturing. *Int J Adv Manuf Technol*. <https://doi.org/10.1007/s00170-020-06563-5>
- [54] van Dam J, van MOURIK P (2017) *Materials science in design and engineering*. Delft Academic Press, [S.l.]
- [55] Tekkaya AE (2001) Improved relationship between Vickers hardness and yield stress for cold formed materials. *Steel Res*. <https://doi.org/10.1002/srin.200100122>
- [56] Busby JT, Hash MC, Was GS (2005) The relationship between hardness and yield stress in irradiated austenitic and ferritic steels. *J Nucl Mater*. <https://doi.org/10.1016/j.jnucmat.2004.09.024>
- [57] Hashemi SH (2011) Strength–hardness statistical correlation in API X65 steel. *Mater Sci Eng A*. <https://doi.org/10.1016/j.msea.2010.10.089>
- [58] Khodabakhshi F, Haghshenas M, Eskandari H, Koohbor B (2015) Hardness–strength relationships in fine and ultra-fine grained metals processed through constrained groove pressing. *Mater Sci Eng A*. <https://doi.org/10.1016/j.msea.2015.03.122>
- [59] Zhang P, Li SX, Zhang ZF (2011) General relationship between strength and hardness. *Mater Sci Eng A*. <https://doi.org/10.1016/j.msea.2011.08.061>
- [60] Childs T, Hauser C, Badrossamay M (2004) Mapping and modelling single scan track formation in direct metal selective laser melting. *CIRP Ann*. [https://doi.org/10.1016/S0007-8506\(07\)60676-3](https://doi.org/10.1016/S0007-8506(07)60676-3)
- [61] Chandrasekhar S (2013) *Hydrodynamic and hydromagnetic stability*. Dover Publications Inc, New York
- [62] Yadroitsev I, Gusarov A, Yadroitsava I, Smurov I (2010) Single track formation in selective laser melting of metal powders. *J Mater Process Technol*. <https://doi.org/10.1016/j.jmatprotec.2010.05.010>
- [63] Lide DR (ed) (1994) *CRC handbook of chemistry and physics: a ready-reference book of chemical and physical data*, 75th edn. CRC Press, Boca Raton
- [64] Ji X, Zhang S, Wang Y, Liang SY (2022) Effect of thermal-fluidic transport on the temperature distribution and the melt pool in laser powder bed fusion of Ti6Al4V. *Opt Laser Technol*. <https://doi.org/10.1016/j.optlastec.2022.108587>
- [65] Takata N, Liu M, Li H, Suzuki A, Kobashi M (2022) Fast scanning calorimetry study of Al alloy powder for understanding microstructural development in laser powder bed fusion. *Mater Des*. <https://doi.org/10.1016/j.matdes.2022.110830>
- [66] Pfaff A, Schäffer S, Jäcklein M, Balle F (2023) Measuring the cooling behavior of melt pools in L-PBF by pyrometry. *Materials*. <https://doi.org/10.3390/ma16103647>
- [67] Promopattum P, Yao S-C, Pistorius PC, Rollett AD, Coutts PJ, Lia F, Martukanitz R (2018) Numerical modeling and experimental validation of thermal history and microstructure for additive manufacturing of an Inconel 718 product. *Prog Addit Manuf*. <https://doi.org/10.1007/s40964-018-0039-1>
- [68] ScipioniBertoli U, Guss G, Wu S, Matthews MJ, Schoenung JM (2017) In-situ characterization of laser-powder interaction and cooling rates through high-speed imaging of powder bed fusion additive manufacturing. *Mater Des*. <https://doi.org/10.1016/j.matdes.2017.09.044>
- [69] Chae H, Huang E-W, Woo W, Kang SH, Jain J, An K, Lee SY (2021) Unravelling thermal history during additive manufacturing of martensitic stainless steel. *J Alloy Compd*. <https://doi.org/10.1016/j.jallcom.2020.157555>
- [70] Farshidianfar MH, Khajepour A, Gerlich AP (2016) Effect of real-time cooling rate on microstructure in laser additive

manufacturing. *J Mater Process Technol.* <https://doi.org/10.1016/j.jmatprotec.2016.01.017>

[71] Oettel H (ed) (2011) *Metallografie: Mit einer Einführung in die Keramografie*, 15th edn. Master. Wiley-VCH, Weinheim

[72] Źrodowski Ł, Wysocki B, Wróblewski R, Krawczyńska A, Adamczyk-Cieślak B, Zdunek J, Błyskun P, Ferenc J, Leonowicz M, Świążkowski W (2019) New approach to amorphization of alloys with low glass forming ability via

selective laser melting. *J Alloy Compd.* <https://doi.org/10.1016/j.jallcom.2018.08.075>

Publisher's Note Springer Nature remains neutral with regard to jurisdictional claims in published maps and institutional affiliations.